

ARTICLE

Received 26 Dec 2016 | Accepted 17 May 2017 | Published 3 Jul 2017

DOI: 10.1038/ncomms15975

OPEN

Scanning tunnelling spectroscopy of superconductivity on surfaces of $\text{LiTi}_2\text{O}_4(111)$ thin films

Yoshinori Okada¹, Yasunobu Ando^{2,3}, Ryota Shimizu¹, Emi Minamitani², Susumu Shiraki¹, Satoshi Watanabe² & Taro Hitosugi^{1,4}

Unique superconductivity at surfaces/interfaces, as exemplified by $\text{LaAlO}_3/\text{SrTiO}_3$ interfaces, and the high transition temperature in ultrathin FeSe films, have triggered intense debates on how superconductivity is affected in atomic and electronic reconstructions. The surface of superconducting cubic spinel oxide LiTi_2O_4 is another interesting system because its inherent surface electronic and atomic reconstructions add complexity to superconducting properties. Investigations of such surfaces are hampered by the lack of single crystals or high-quality thin films. Here, using low-temperature scanning tunnelling microscopy and spectroscopy, we report an unexpected small superconducting energy gap and a long coherence length on the surface of $\text{LiTi}_2\text{O}_4(111)$ epitaxial thin films. Furthermore, we find that a pseudogap opening at the Fermi energy modifies the surface superconductivity. Our results open an avenue for exploring anomalous superconductivity on the surface of cubic transition-metal oxides, where the electronic states are spontaneously modulated involving rich many-body interactions.

¹Advanced Institute for Materials Research, Tohoku University, Sendai 980-8577, Japan. ²Department of Materials Engineering, The University of Tokyo, Tokyo 113-8656, Japan. ³Research Center for Computational Design and Advanced Functional Materials, National Institute for Advanced Science and Technology, Tsukuba, Ibaraki 305-8568, Japan. ⁴School of Materials and Chemical Technology, Tokyo Institute of Technology, Tokyo 152-8552, Japan. Correspondence and requests for materials should be addressed to Y.O. (email: yoshinori.okada@wpi-aimr.tohoku.ac.jp) or to Y.A. (email: yasunobu.ando@aist.go.jp).

Recent advances in the atomic-scale synthesis and characterization of two-dimensional superconductors have kindled significant interest in their exotic electronic, orbital and magnetic structures^{1–6}. In addition to the ultrathin superconducting films on substrates^{7–20}, surfaces of cubic-structure superconducting transition-metal oxides provide another interesting platform, because the spontaneous electronic and atomic reconstructions on surfaces are expected to modify superconductivity. A particularly interesting system is the spinel oxide (AB_2O_4) superconductor. In this system, the cubic pyrochlore sublattice of B -atoms provides large degeneracy (frustration) of charge, spin and orbital states in bulk^{21,22}, and a prominent degeneracy lifting at the surface is expected to lead rich electronic states on the surface. None of the previous studies, however, has revealed the electronic signature of modulated superconductivity on their surfaces.

Lithium titanate, $LiTi_2O_4$, is the only oxide superconductor with spinel structure^{23–26}, and exhibits the highest superconducting transition temperature (T_c) with ~ 13.7 K of any spinel superconductors^{27–32}. It is known as a $3d^{0.5}$ metallic system (one half of an electron per Ti atom resides in the $3d$ states), and medium-coupling Bardeen–Cooper–Schrieffer (BCS) superconductivity with s -wave pairing symmetry has been proposed^{33–36}. Recent transport data with epitaxial films showed an angle-dependent anomalous magnetoresistance, which is possibly related to a spin and orbital fluctuation effect²². On the basis of this data, the similarity between $LiTi_2O_4$ and high T_c cuprates has been discussed²². Although superconducting properties of bulk $LiTi_2O_4$ have been investigated extensively, studies of the superconductivity at $LiTi_2O_4$ surfaces have been hindered by the lack of single crystals and high-quality thin films. Recently, high-quality epitaxial $LiTi_2O_4$ thin films were successfully grown using pulsed laser deposition (PLD)^{37–39}; however, investigations of the superconductivity on $LiTi_2O_4$ surfaces remain unexplored. Recently, we have developed a scanning tunnelling microscope (STM) combined with a PLD system⁴⁰, and *in situ* investigation of the $LiTi_2O_4$ surface without exposing to air has become possible.

Here we report modified superconductivity at the surfaces of $LiTi_2O_4(111)$ epitaxial thin films, using STM/scanning tunnelling spectroscopy (STM/STS) and first-principles density functional theory (DFT) calculations. From the atomic-scale observations of superconductivity, we present measurements of the unexpected small superconducting energy gap Δ and a long coherence length ξ values. Furthermore, we found that a superconducting gap exists on large energy scale pseudogap states. These results provide the spectroscopic evidence of spontaneous superconducting modification on the surface of cubic transition-metal oxides, paving an interesting path to explore exotic superconductivity involving rich interactions.

Results

Preparation of higher T_c sample with flat surface. We found that low-temperature film deposition using PLD followed by post-deposition annealing increases T_c up to 13 K, together with improved surface flatness. We first compare the STM images of the films grown at substrate temperature T_s of 600 °C (Fig. 1a) and 400 °C (Fig. 1b). The former temperature is the typical growth temperature reported in the previous studies^{22,37–39}. While many triangular-shaped islands are observed on both surfaces, the height of the islands is much smaller in the latter film, indicating that the surface roughness is strongly dependent on the growth temperatures. As the T_s is reduced from 600 to 400 °C, the root mean square (RMS) value of surface roughness,

R_{RMS} , improved from 0.86 (Fig. 1a) to 0.40 nm (Fig. 1b). To further improve the surface roughness, we investigated the post-deposition annealing effect on the film grown at $T_s = 400$ °C; thin films were annealed at 600 °C in ultrahigh vacuum for an hour. Expectedly, the film became flatter to $R_{RMS} = 0.28$ nm (Fig. 1c). Furthermore, this R_{RMS} value was improved to 0.21 nm for the film deposited at $T_s = 300$ °C followed by the above-mentioned annealing (Fig. 1d and Supplementary Fig. 1).

Importantly, this annealing process increases T_c values (Fig. 1f), in addition to the flattening of the surfaces. While the T_c values of the films grown at $T_s = 500$ and 600 °C show 12.0 K and 12.5 K, respectively, the T_c increases up to 13.0 K for the films after annealing (red curves in Fig. 1f). The T_c value of ~ 13 K is one of the highest values among reported values for $LiTi_2O_4$ epitaxial thin films^{22,37–39}. We confirmed from X-ray diffraction that the films exhibit rocking-curve full-width at half-maximum of 0.36° for 444 peak, and that the lattice is fully relaxed from $SrTiO_3(111)$ substrate (Supplementary Fig. 2). The above results show that the quality of the sample is quite high. In the following investigations, we focus on the films deposited at $T_s = 300$ °C followed by the post-deposition annealing in vacuum at 600 °C.

Atomic-scale order on $LiTi_2O_4(111)$ film surface. We observed, on the atomic level, a well-ordered triangular lattices and defects. Figure 2a shows the wide-area STM image of the $LiTi_2O_4$ surface, where flat terraces and dark spots with peculiar defect shapes were observed. In the close-up image (Fig. 2c), strong topographic corrugations (shown in blue) are observed together with weak topographic corrugations (shown in red), displaying three-fold symmetry. This is consistent with the inherent three-fold rotational symmetry along the $[111]$ axis in a spinel system. The unit cell size was found to be ~ 0.6 nm (Fig. 2c), which was independent of the location and sample-bias voltages V_s . This size well matches that of the unit cell of $LiTi_2O_4$ bulk (111) plane. We concluded that the protrusions of the triangular lattice originate from Ti atoms on the surface, as discussed later together with the nature of the defects (dark spots).

Superconductivity in tunnelling spectra measurements. In addition to the atomic-scale corrugations, we observed clear signature of superconductivity in tunnelling spectra measurements at 4.2 K. The wide- and narrow-energy-range spectra were obtained at the area far from defects (see cross in Fig. 3a). To evaluate the superconducting gap Δ quantitatively, we analysed tunnelling spectra (Fig. 3b–d) using the Dynes formula⁴¹ convoluted with an energy derivative of the Fermi–Dirac function F .

$$\frac{dI}{dV}(eV_s, T) = \int_{-\infty}^{+\infty} \left\{ \frac{dF(E + eV_s, T)}{dE} \right\} \times (a + bE) \times \text{Re} \left\{ \frac{E - i\Gamma}{\sqrt{(E - i\Gamma)^2 - \Delta^2}} \right\} dE \quad (1)$$

Here we assume that the normal-state density of states (DOS) near E_F has a linear dependence with energy E , expressed as $(a + bE)$, and Γ is the spectral broadening factor. The fitting parameters a , b , Δ and Γ are determined with fixed temperature $T = 4.2$ K. We fitted our spectra (Fig. 3d) with a single-component isotropic pairing gap, and we obtained $\Delta = 1.716 \pm 0.004$ meV and $\Gamma = 0.321 \pm 0.004$ meV. According to the BCS gap function, assuming the same T_c for surfaces and bulk (13 K), the obtained Δ value can be regarded as a gap value in the $T = 0$ K limit. With using bulk T_c , the obtained $2\Delta/k_B T_c$ value of 3.0 is unexpectedly small. In contrast, the $2\Delta/k_B T_c$ values reported in polycrystalline

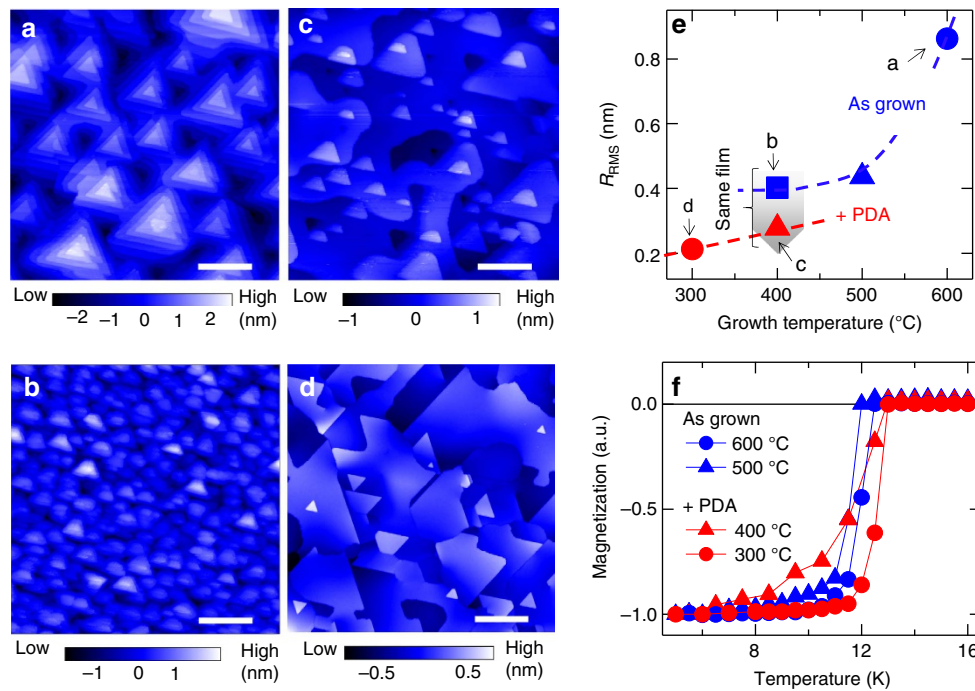


Figure 1 | Surface topographies and superconducting critical temperatures. (a,b) STM topographic images of as-deposited thin film at substrate temperature of 600 °C (a) and 400 °C (b). (c,d) STM images after post-deposition annealing (PDA) for films deposited at 400 °C (c) and 300 °C (d). Note that b,c are taken with using the same film. a-c are obtained at 77 K and d is obtained at 4.2 K (all the STM images were observed at a sample-bias voltage of +300 mV and a tunnelling current is about 10 pA). Scale bar, 80 nm (a-d). (e) Growth temperature dependence of root mean square of surface roughness (R_{RMS}) values: as-grown samples (blue symbols) and after PDA (red symbols). The value of R_{RMS} is evaluated from topographic images observed at a sample-bias voltage of +300 mV and a tunnelling current of 10 pA (scan area of 400 nm). (f) Temperature dependence of the field-cooled dc magnetic susceptibility for the LiTi_2O_4 films in a magnetic field of 50 Oe, which was applied parallel to the (111) plane. Clear diamagnetism is observed.

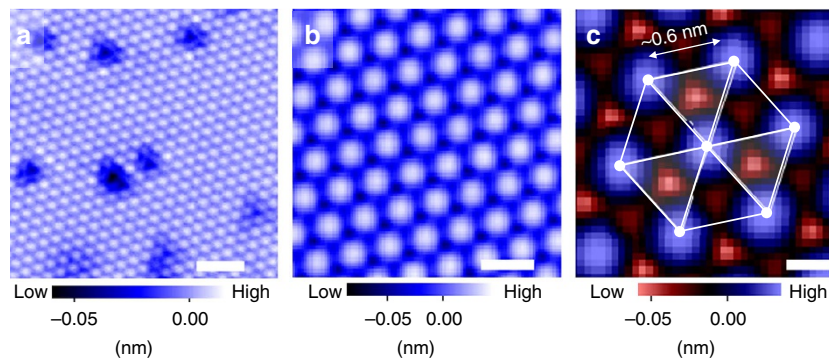


Figure 2 | Typical topographic images on a terrace. (a) Filled-state STM image of $\text{LiTi}_2\text{O}_4(111)$ surface (11.6 nm \times 11.6 nm, sample-bias voltage V_s of -900 mV, tunnelling current I_{set} of 30 pA). (b) Empty-state STM image (4 nm \times 4 nm, $V_s = +30$ mV, $I_{set} = 30$ pA). (c) Zoomed-up image (1.7 nm \times 1.7 nm, $V_s = +30$ mV, $I_{set} = 30$ pA) of b. The image shows three-fold symmetry representing the spinel crystal structure. Scale bars, 2 nm (a), 0.8 nm (b) and 0.3 nm (c).

LiTi_2O_4 samples range from 3.5 to 4.0 in point-contact spectroscopy^{33,34} and Andreev reflection³⁶. A recent report using epitaxial LiTi_2O_4 thin films claims $2\Delta/k_B T_c = 4.07$ from point-contact spectroscopy²², and thus the obtained value of 3.0 is much smaller than that of all the previous reports. Furthermore, the present value is even smaller than that for the weak coupling limit for s -wave BCS superconductivity of 3.52. We discuss later the possible origins of this unexpectedly small $2\Delta/k_B T_c$.

Coherence length on the surface. To further study the superconductivity on the surface, we investigated the value of ξ from the electronic structures around a magnetic vortex core. We first analysed the V_s dependent conductance (dI/dV) map around a

single vortex core by applying an external magnetic field of 1.5 T perpendicular to the surface at 4.2 K (Fig. 4a-e). At $V_s = -8$ mV and $+8$ mV, we observed uniform conductance over the scanned region (Fig. 4a,e), whereas conductance values were depressed around the centre of images at $V_s = -4$ mV and $+4$ mV (Fig. 4b,d). This depressed conductance is a consequence of suppressed coherence peaks. In contrast, the conductance map at $V_s = 0$ mV clearly represents enhanced conductance in the centre region (Fig. 4c). This enhanced zero-bias conductance around the centre region is because of pair breaking. These energy evolutions of conductance map indicate signatures of a vortex core (Fig. 4a-e), and the evolution of tunnelling spectra along line A-B in Fig. 4a clearly shows a typical spatial evolution of spectral shape across a vortex core (Fig. 4f).

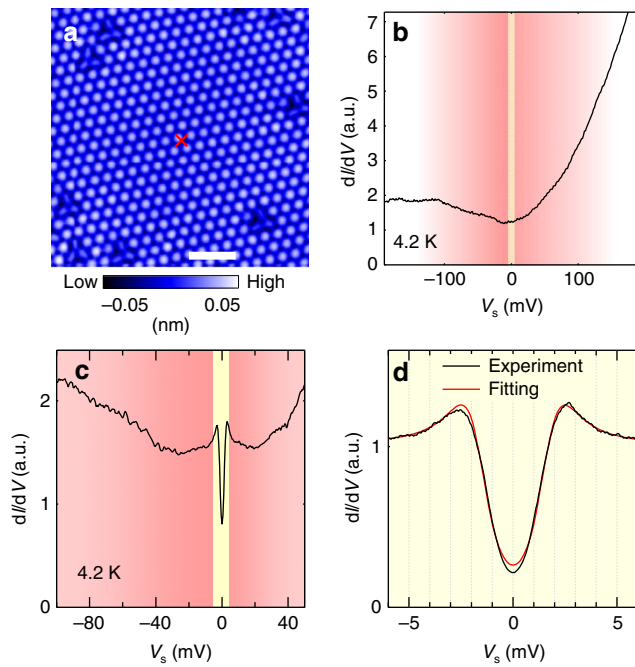


Figure 3 | Tunneling spectra obtained away from defects.

(a) A topographic image obtained with a sample-bias voltage V_s of +30 mV and a tunnelling current of 30 pA. Scale bar, 2 nm. The red cross in **a** indicates the position where the spectra shown in **b-d** were obtained. (b,c) Tunnelling spectrum (dI/dV) obtained at a wide energy region (V_s of -190 mV to $+190$ mV and -100 mV to $+50$ mV, for **a,b**, respectively.) (c) High-resolution tunnelling spectrum for V_s between ± 6 mV near the Fermi energy. Experimental curve (black dots) and fitted curve (red line) are shown in the same figure. See main body for the details of the fitting procedure. The energy windows of numerical derivative to obtain conductance spectrum were 15, 1.5 and 0.3 mV for **a-c**, respectively. The yellow region represents the V_s range of -6 to 6 mV. All the images and spectra were obtained at 4.2 K.

To evaluate ξ , we analysed the zero-bias conductance data as a function of the radial distance from the vortex core centre r (Supplementary Fig. 3). We first extracted the zero-bias conductance Z as a function of mean distance r . Then, we fitted the $Z(r)$ by the exponential decay function $Z(r) = Z(\infty) + A \exp(-r/\xi)$, where A is a constant and $Z(\infty)$ is the normalized zero-bias conductance away from the vortex core⁴². From the fitting, we obtained $\xi = 12 \pm 1$ nm (Fig. 4h), $A = 0.505 \pm 0.02$ and $Z(\infty) = 0.512 \pm 0.03$. This ξ value is much larger than the ξ_{GL} values obtained from the upper critical field (H_{c2}) using the formula $H_{c2} = \Phi_0 / 2\pi \xi_{GL}^2$ (Φ_0 is the magnetic flux quanta) based on Ginzburg–Landau theory. For epitaxial LiTi_2O_4 thin films, the ξ_{GL} values estimated from macroscopic measurements are 4.1–4.7 nm (refs 22,37). Whereas excellent agreement between ξ and ξ_{GL} values have been reported in other superconducting systems such as Fe-based superconductors^{42,43}, the values of ξ obtained on the surface of LiTi_2O_4 are much larger than the estimated ξ_{GL} obtained from transport measurement techniques. The deviation of ξ from ξ_{GL} also implies that there is a difference in superconductivity between surface and bulk.

Discussion

To understand the superconductivity on the $\text{LiTi}_2\text{O}_4(111)$ surface, we performed first-principles calculations. We first calculated the bulk electronic structures to understand the triangular lattice observed in the STM images. Figure 5a shows the calculated partial DOS for bulk. The Ti $3d$ states predominantly contribute near E_F , and the influence of Li atoms should be negligible to the STM images. Thus, the main protrusions of the triangular lattice observed in the topographic image (indicated by blue colour in Fig. 2) correspond to Ti atoms on the surface.

To further understand the $\text{LiTi}_2\text{O}_4(111)$ surface, we calculated the electronic structures of four possible bulk-cut surfaces: two-types of O-terminated, Kagome-lattice Ti-terminated, and TiLi_2 -terminated surfaces (see four dotted lines in Fig. 5b). These

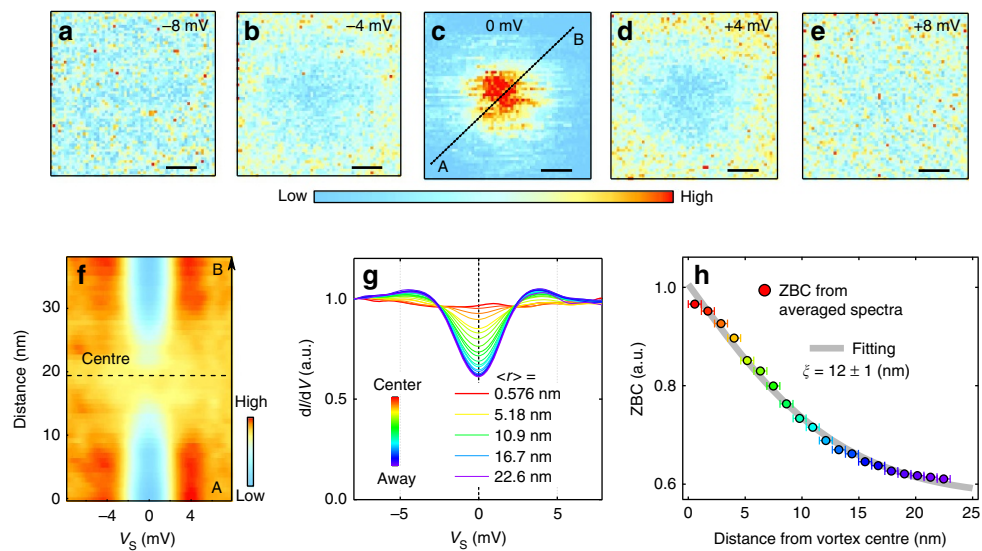


Figure 4 | Spectral evolution around a vortex core. A single vortex core is investigated at the temperature of 4.2 K with applying a magnetic field of 1.5 T normal to the surface. (a–e) Conductance mappings around an isolated single vortex core with various sample-bias voltages. A STM tip is stabilized at a tunnelling current of 30 pA and a sample-bias voltage of -10 mV. The energy window of numerical derivative to obtain conductance spectrum is 1 mV. Scale bars, 6 nm (a–e). (f) Spatial evolution of tunnelling spectra across the vortex centre (the line is shown in c). (g) Averaged spectra as a function of distance from vortex centre $\langle r \rangle$. (h) Zero-bias conductance (ZBC) obtained from g. Coherence length of ~ 12 nm is obtained by fitting the ZBC (see main text for details). A total 3,600 spectra (60×60) were taken with equal spacing in the region (a–e). We classified the area of Fig. 4a–e into 20 regions based on the distance from vortex centre (see also Supplementary Fig. 3). Interval of $\langle r \rangle$, which is 5.758 nm, is set as error bars for x axis in h.

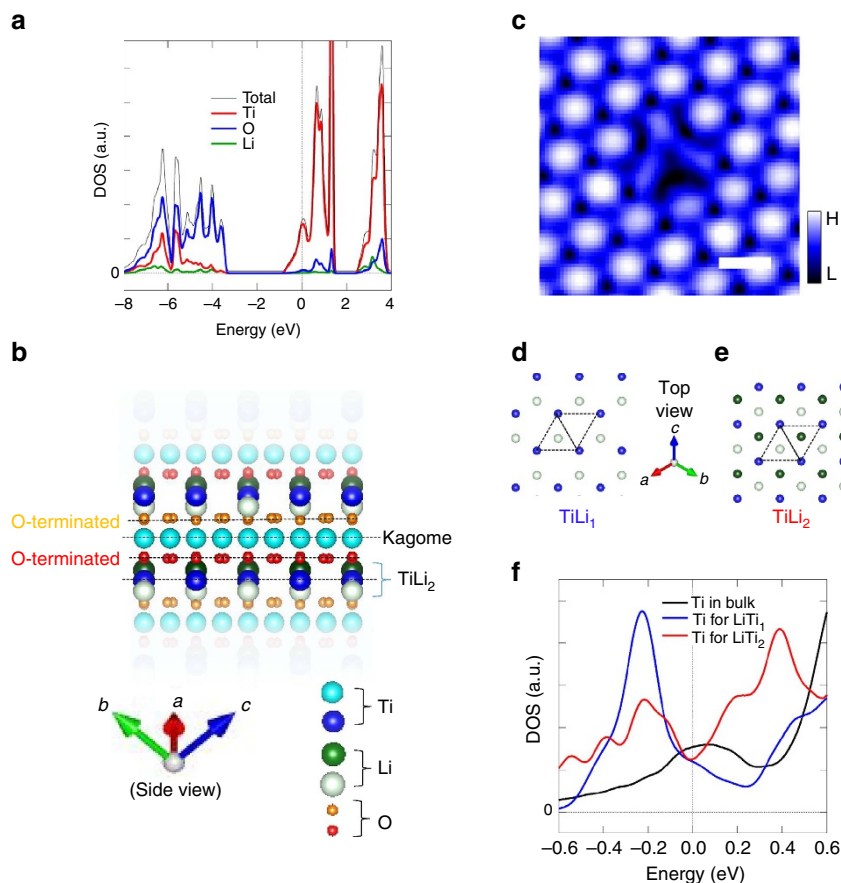


Figure 5 | Comparison between bulk and surface electronic states based on DFT calculations. (a) Calculated DOS for bulk LiTi_2O_4 . (b) Crystal structure with bulk continuum, together with four bulk-cut planes represented by broken lines. Vertical axis is along the (111) crystal orientation. (c) The topographic image of a defect on the surface (a sample-bias voltage of +30 mV, a tunnelling current of 30 pA). Scale bar, 0.6 nm (c). Top view of TiLi_2 - (d) and TiLi_1 - (e) terminated surfaces. See b for the colour of the circles. (f) Calculated DOS for the topmost Ti atoms in TiLi_2 - and TiLi_1 -terminated surfaces. DOS for bulk is shown again for clarity. Here 0 on the horizontal axes in a, f correspond to the Fermi energy.

surfaces were optimized structurally and the electronic states of the reconstructed surfaces were investigated. Both the two O-terminated surfaces resulted in an insulating band structure (Supplementary Fig. 4a,b), which is inconsistent with the experimental metallic tunnelling spectra (Fig. 3). For the Kagome-lattice Ti-terminated surface, the simulated charge density plot (Supplementary Fig. 4c) also shows inconsistency with the experimental topographic image (Fig. 2). Consequently, neither the O-terminated nor the Kagome-lattice Ti-terminated surface reproduced the experimental results (Supplementary Fig. 4). On the other hand, TiLi_2 -terminated surface shows metallic states, and the arrangement of the protrusions and their nearest neighbour distance (0.6 nm) observed in the STM image (Fig. 2) can be explained by the framework of Ti-triangular lattice of TiLi_2 layer.

We focus on the TiLi_2 -terminated surface, and further investigate the effect of Li-layer deficiency near surface since Li may be easily deficient during depositions process due to its high volatility. The TiLi_2 -terminated surface contains a triangular lattice of Ti atoms, and two layers of Li atoms: Li atoms displaced towards the vacuum (hereafter called higher Li layer, dark green circle in Fig. 5b) and those displaced towards the bulk (hereafter called lower Li layer, light green circle in Fig. 5b). Three possible models of surface terminations are considered: a stoichiometric TiLi_2 -terminated surface, a surface without the higher Li layer (TiLi_1 -terminated surface), and a surface without both higher and lower Li layer (TiLi_0 -terminated surface) (Fig. 5b).

On the basis of the following discussion, we could exclude TiLi_0 -terminated surface by showing that Li atoms reside at the vicinity of the topmost Ti-triangular lattice. Figure 5c shows a close-up image of the dark spots observed in the wide-area STM image (Fig. 3a). Three oval protrusions are observed, and this image indicates that a defect centre is around the middle of the three oval protrusions. Considering that the ovals are at the Ti sites, and taking into account the crystal structure of spinel system, the defects could be identified as a point-Li defect. Indeed, the dark contrast around this point-Li defect, observed at a negative sample-bias voltage of -900 meV, is consistent with hole-doping nature of Li vacancy (Fig. 2a). These results demonstrate that Li atoms reside at the vicinity of the topmost Ti-triangular lattice. Accordingly, the results exclude TiLi_0 termination, and the surface of the films is terminated with either TiLi_2 or TiLi_1 structure. We note that the density of point-Li defects on the surface is <2% of Li atoms. Thus, we speculate that the impact of the presence of point-Li defects on superconductivity can be negligible²⁵, unless the defects on the surfaces induce local magnetic moments.

We now compare the DOS at E_F , $N(E_F)$, of a bulk and that of the TiLi_2 - and TiLi_1 - terminated surfaces, and reveal that both surfaces have smaller $N(E_F)$ than that of the bulk. Our DFT calculations for bulk show a peak structure at E_F (Fig. 5a), which is consistent with previous calculations using the linear muffin-tin orbital method⁴⁴ and full-potential linearized augmented plane wave⁴⁵. The simulated peak structure at E_F is also consistent with

an experimental report of large normal-state electronic-specific heat, which is a measure of $N(E_F)$ for bulk³⁵. On the TiLi_2 - (Fig. 5d) and TiLi_1 - (Fig. 5e) terminated surfaces, a broken lattice symmetry normal to the surface lifts the degeneracy of the t_{2g} orbitals and modifies the orbital states on the surface. Compared to the bulk, we observed reduction of the $N(E_F)$ at the topmost Ti atoms for both TiLi_2 and TiLi_1 (Fig. 5f). Because the smaller $N(E_F)$ leads to lower T_c according to the BCS theory, the calculation naively suggest suppressed superconductivity on the surface.

Based on the above discussions, we present here coherent interpretation of the experimental results. As we experimentally observed a pseudogap state (shaded red in Fig. 3a,b), which is expected to be absent in bulk, the modified superconductivity on the surface is a reasonable hypothesis. Indeed, using bulk T_c and surface Δ , the $2\Delta/k_B T_c$ value becomes anomalously small. This is puzzling since the value 3.0 is much smaller than that for a weak coupling limit of BCS superconductors (3.52). However, this puzzle can be explained by considering the presence of a non-superconducting or reduced- T_c surface layer. Moreover, the large ξ value can possibly be understood as the reduced $N(E_F)$ due to pseudogap formation on the surface. The Fermi velocity v_F is proportional to $1/N(E_F)$; therefore, based on the formula $\xi = v_F/D$ derived from BCS theory, the larger v_F together with smaller D on a surface increases ξ more than that for the bulk value. Beyond the framework of the less-interacting picture, it is an interesting future subject to investigate relations between modified superconductivity, pseudogap formation and frustration effects on this (111) oriented spinel oxide surface.

In summary, we have investigated superconductivity in the atomically well-defined surface of $\text{LiTi}_2\text{O}_4(111)$ thin films, using STM/STS and first-principles calculations. We provided spectroscopic evidence of modified superconductivity on the surface, originating from the formation of a pseudogap in the DOS. Our study has made an essential first step towards exploring superconducting phenomena emerging from spontaneous atomic and electronic reconstruction on surfaces, including different film orientation⁴⁶, of superconducting cubic transition-metal oxides.

Methods

Samples and characterizations. We used a low-temperature STM connected with a PLD chamber. This system enables us to investigate thin film surfaces immediately after their deposition, without exposing surfaces to air. The base pressure of the PLD chamber was 5×10^{-11} Torr. Thin films of LiTi_2O_4 are grown on Nb(0.05 wt %) doped $\text{SrTiO}_3(111)$ substrate using PLD with a KrF excimer laser (wavelength $\lambda = 248$ nm). We used $\text{Li}_4\text{Ti}_5\text{O}_{12}$ target for PLD film growth to compensate the Li loss during depositions. Substrates were annealed at 1,000 °C for an hour in oxygen under a partial pressure $P_{\text{O}_2} = 5 \times 10^{-7}$ Torr before film depositions. Substrates were resistively heated, and their temperatures were monitored using a pyrometer. We deposited film at a substrate temperature $T_s = 300$ °C under $P_{\text{O}_2} = 5 \times 10^{-7}$ Torr followed by post-deposition annealing at 600 °C in ultrahigh vacuum for one hour. During thin film depositions, pulse repetition and fluence were set at 2 Hz and 1 J cm^{-2} , respectively. Film thickness, measured *ex situ* using a DEKTAK 3030ST mechanical profiler, was determined to be about 100 nm. The STM data shown in Fig. 1a-c were taken at liquid-nitrogen temperature (77 K). The rest of STM data were taken at liquid-helium temperature (4.2 K). We obtained differential conductance values (dI/dV) from the numerical derivatives of I (tunnelling current) – V (voltage) curves. For *ex situ* characterization, we measured X-ray diffraction pattern and temperature dependence of magnetization after *in situ* STM/STS measurements.

First-principles calculations. For the first-principles calculations, we used DFT with the code Quantum ESPRESSO, with the generalized gradient approximation and ultra-soft pseudopotential scheme^{47–51}. Cutoff energies for the Kohn–Sham orbitals and charge density of 32.5 and 45 Ry are imposed. The Brillouin-zone summation is evaluated using $3 \times 3 \times 1$ and $12 \times 12 \times 1$ k -point sampling for the structure optimizations and the DOS calculations, respectively. For the DOS broadening, we applied a simple Gaussian broadening method with broadening parameter of 0.005 Ry. Convergence criteria of the structure optimization are 10×10^{-3} for forces and 10×10^{-4} for energy. For the calculation of the near-surface atomic/electronic structures, we use the symmetric slab model with

four unit cells along the (111) direction on each side. In the structure optimization, the topmost surface structures are initiated from bulk cuts. The atomic positions of the Ti atoms at the centre of the symmetric slab model along the (111) direction are fixed during optimization. Spin degrees of freedom and electron–electron correlations are not included in the calculation.

Data availability. The data that support the findings of this study are available from the corresponding authors on reasonable request.

References

- Bozovic, I., Logvenov, G., Belca, I., Narimbetov, B. & Sveklo, I. Epitaxial strain and superconductivity in $\text{La}_{2-x}\text{Sr}_x\text{CuO}_4$ thin films. *Phys. Rev. Lett.* **89**, 107001 (2002).
- Gozar, A. *et al.* High-temperature interface superconductivity between metallic and insulating copper oxides. *Nature* **455**, 782–785 (2008).
- Bert, J. A. *et al.* Direct imaging of the coexistence of ferromagnetism and superconductivity at the $\text{LaAlO}_3/\text{SrTiO}_3$ interface. *Nat. Phys.* **7**, 767–771 (2011).
- Li, L., Richter, C., Mannhart, J. & Ashoori, R. C. Coexistence of magnetic order and two-dimensional superconductivity at $\text{LaAlO}_3/\text{SrTiO}_3$ interfaces. *Nat. Phys.* **7**, 762–766 (2011).
- Scheurer, M. S. & Schmalian, J. Topological superconductivity and unconventional pairing in oxide interfaces. *Nat. Commun.* **6**, 6005 (2014).
- Gor'kov, L. P. & Rashba, E. I. Superconducting 2D system with lifted spin degeneracy: mixed singlet-triplet state. *Phys. Rev. Lett.* **87**, 037004 (2001).
- Liu, D. *et al.* Electronic origin of high-temperature superconductivity in single-layer FeSe superconductor. *Nat. Commun.* **3**, 931 (2012).
- Ge, J. F. *et al.* Superconductivity above 100 K in single-layer FeSe films on doped SrTiO_3 . *Nat. Mater.* **14**, 285–289 (2015).
- Shiogai, J., Ito, Y., Mitsuhashi, T., Nojima, T. & Tsukazaki, A. Electric-field-induced superconductivity in electrochemically etched ultrathin FeSe films on SrTiO_3 and MgO. *Nat. Phys.* **12**, 42–46 (2016).
- Miyata, Y., Nakayama, K., Sugawara, K., Sato, T. & Takahashi, T. High-temperature superconductivity in potassium-coated multilayer FeSe thin films. *Nat. Mater.* **14**, 775–779 (2015).
- Guo, Y. *et al.* Superconductivity modulated by quantum size effects. *Science* **306**, 1915 (2004).
- Qin, S., Kim, J., Niu, Q. & Shih, C. K. Superconductivity at the two-dimensional limit. *Science* **324**, 1314–1317 (2009).
- Nishio, T., Ono, M., Eguchi, T., Sakata, H. & Hasegawa, Y. Superconductivity of nanometer-size Pb islands studied by low-temperature scanning tunneling microscopy. *Appl. Phys. Lett.* **88**, 113115 (2006).
- Zhang, T. *et al.* Superconductivity in one-atomic-layer metal films grown on $\text{Si}(111)$. *Nat. Phys.* **6**, 104 (2010).
- Uchihashi, T., Mishra, P., Aono, M. & Nakayama, T. Macroscopic superconducting current through a silicon surface reconstruction with indium adatoms: $\text{Si}(111) - (\sqrt{7} \times \sqrt{3}) - \text{In}$. *Phys. Rev. Lett.* **107**, 207001 (2011).
- Yoshizawa, S. *et al.* Imaging Josephson vortices on the surface superconductor $\text{Si}(111) - (\sqrt{7} \times \sqrt{3}) - \text{In}$ using a scanning tunneling microscope. *Phys. Rev. Lett.* **113**, 247004 (2014).
- Brun, C. *et al.* Remarkable effects of disorder on superconductivity of single atomic layers of lead on silicon. *Nat. Phys.* **10**, 444–450 (2014).
- Joe, Y. I., Abbamonte, P. & Geck, J. Orbital textures and charge density waves in transition-metal dichalcogenides. *Nat. Phys.* **11**, 328–331 (2015).
- Xi, X. *et al.* Ising pairing in superconducting NbSe_2 atomic layers. *Nat. Phys.* **12**, 139–143 (2016).
- Lu, J. M. *et al.* Evidence for two-dimensional Ising superconductivity in gated MoS_2 . *Science* **350**, 1353–1357 (2015).
- Lee, S. *et al.* Frustrated magnetism and cooperative phase transitions in spinels. *J. Phys. Soc. Japan* **79**, 011004 (2010).
- Jin, K. *et al.* Anomalous magnetoresistance in the spinel superconductor LiTi_2O_4 . *Nat. Commun.* **6**, 7183 (2015).
- Bragg, W. The structure of magnetite and the spinels. *Nature* **95**, 561–561 (1915).
- Johnston, D. C., Prakash, H. & Zachariasen, W. H. High temperature superconductivity in Li-Ti-O ternary system. *Mat. Res. Bull.* **8**, 777–784 (1973).
- Johnston, D. C. Superconducting and normal state properties of $\text{Li}_{1+x}\text{Ti}_{2-x}\text{O}_4$ spinel compounds. I. Preparation, crystallography, superconducting properties, electrical resistivity, dielectric behavior, and magnetic susceptibility. *J. Low Temp. Phys.* **25**, 145 (1976).
- Callum, R. W., Johnston, D. C., Luengo, C. A. & Maple, M. P. Superconducting and normal state properties of $\text{Li}_{1+x}\text{Ti}_{2-x}\text{O}_4$ spinel compounds. II. Low-temperature heat capacity. *J. Low Temp. Phys.* **25**, 177 (1976).
- Robbins, M., Willens, R. H. & Miller, R. C. Superconductivity in the spinels CuRh_2S_4 and CuRh_2Se_4 . *Solid State Commun.* **5**, 933 (1967).
- Shelton, R. N., Johnston, D. C. & Adrian, H. Measurement of the pressure dependence of T_c for superconducting spinel compounds. *Solid State Commun.* **20**, 1077 (1976).

29. Hagino, T. *et al.* Superconductivity in spinel-type compounds CuRh_2S_4 and CuRh_2Se_4 . *Phys. Rev. B* **51**, 12673 (1995).
30. Ito, M. *et al.* Pressure-induced superconductor-insulator transition in the spinel compound CuRh_2S_4 . *Phys. Rev. Lett.* **91**, 077001 (2003).
31. Cao, G. *et al.* Suppression of metal-to-insulator transition and appearance of superconductivity in $\text{Cu}_{1-x}\text{Zn}_x\text{Ir}_2\text{S}_4$. *Phys. Rev. B* **64**, 214514 (2001).
32. Luo, H. *et al.* Superconductivity in the $\text{Cu}(\text{Ir}_{1-x}\text{Pt}_x)_2\text{Se}_4$ spinel. *Phys. Rev. B* **87**, 214510 (2013).
33. Ng, K. W., Khim, Z. G., Shum, D. P. & Wolf, E. L. Vacuum tunneling spectroscopy of this film and bulk polycrystalline superconductors. *Surf. Sci.* **181**, 37–45 (1987).
34. Ekino, T. & Akimitsu, J. Superconducting energy gap in spinel compound $\text{Li}_{1+x}\text{Ti}_{2-x}\text{O}_4$ from electron tunneling. *Physica B* **165**, 1599 (1990).
35. Sun, C. P. *et al.* Magnetic field dependence of low-temperature specific heat of the spinel oxide superconductor LiTi_2O_4 . *Phys. Rev. B* **70**, 054519 (2004).
36. Tang, L. *et al.* Electrical resistivity and Andreev reflection spectroscopy of the superconducting oxide spinel LiTi_2O_4 . *Phys. Rev. B* **73**, 184521 (2006).
37. Chopdekar, R. V., Wong, F. J., Takamura, Y., Arenholz, E. & Suzuki, Y. Growth and characterization of superconducting spinel oxide LiTi_2O_4 thin films. *Physica C* **469**, 1885–1891 (2009).
38. Kumatani, A. *et al.* Growth processes of lithium titanate thin films deposited by using pulsed laser deposition. *Appl. Phys. Lett.* **101**, 123103 (2012).
39. Oshima, T., Niwa, M., Yokoyama, K. & Ohtomo, A. Pulsed-laser deposition of superconducting LiTi_2O_4 ultrathin films. *J. Cryst. Growth* **419**, 153–157 (2015).
40. Iwaya, K., Shimizu, R., Hashizume, T. & Hitosugi, T. Systematic analyzes of vibration noise of a vibration isolation system for high-resolution scanning tunneling microscopes. *Rev. Sci. Instrum.* **82**, 083702 (2011).
41. Dynes, R. C., Narayanamurti, V. & Garno, J. P. Direct measurement of quasiparticle-lifetime broadening in a strong-coupled superconductor. *Phys. Rev. Lett.* **41**, 1509 (1978).
42. Song, C. L. *et al.* Suppression of superconductivity by twin boundaries in FeSe. *Phys. Rev. Lett.* **109**, 137004 (2012).
43. Song, C. L. *et al.* Dopant clustering, electronic inhomogeneity, and vortex pinning in iron-based superconductors. *Phys. Rev. B* **87**, 214519 (2013).
44. Satpathy, S. & Martini, R. M. Electronic structure of the superconducting oxide spinel LiTi_2O_4 . *Phys. Rev. B* **36**, 7269 (1987).
45. Massidda, S., Yu, J. & Freeman, A. J. Electronic structure and properties of superconducting LiTi_2O_4 . *Phys. Rev. B* **38**, 11352 (1988).
46. He, G. *et al.* Anisotropic electron-phonon coupling in the spinel oxide superconductor LiTi_2O_4 . *Phys. Rev. B* **95**, 054510 (2017).
47. Giannozzi, P. *et al.* Quantum espresso. *J. Phys. Condens. Matter* **21**, 395502 (2009).
48. Hohenberg, P. & Kohn, W. Inhomogeneous electron gas. *Phys. Rev. B* **136**, B864 (1964).
49. Kohn, W. & Sham, L. J. Self-consistent equations including exchange and correlation effects. *Phys. Rev.* **140**, 1133 (1965).
50. Vanderbilt, D. Soft self-consistent pseudopotentials in a generalized eigenvalue formalism. *Phys. Rev. B* **41**, 7892 (1990).
51. Perdew, J. P., Burke, K. & Ernzerhof, M. Generalized gradient approximation made simple. *Phys. Rev. Lett.* **77**, 3865 (1996).

Acknowledgements

We thank Y. Takagi and K. Yamamoto for experimental assistance, and T. Hanaguri, T. Machida, Y. Yoshida, H. Kawasoko and K. Sato for useful discussions. Y.O. acknowledges funding from JSPS KAKENHI Grant Nos. 26707016 and 25886004. T.H. acknowledges funding from JSPS KAKENHI Grant Nos. 26246022, 26106502, 26108702, 26610092, JST-PRESTO and JST-CREST programme. S.W. acknowledges funding from JSPS KAKENHI Grant No. 15H03561. This work was supported by the World Premier Research Center Initiative (WPI), promoted by the Ministry of Education, Culture, Sports, Science and Technology (MEXT) of Japan. We thank P. Han for the critical reading of this manuscript.

Author contributions

Y.O. pursued film growth, STM/STS measurements and data analysis. Y.A. performed the first-principles calculations. Y.O., R.S., S.S. and T.H. discussed the experimental results. Y.A., E.M. and S.W. discussed the theoretical calculations. All authors discussed the conclusions of this paper. Y.O. and T.H. wrote the paper.

Additional information

Supplementary Information accompanies this paper at <http://www.nature.com/naturecommunications>

Competing interests: The authors declare no competing financial interests.

Reprints and permission information is available online at <http://npg.nature.com/reprintsandpermissions/>

How to cite this article: Okada, Y. *et al.* Scanning tunnelling spectroscopy of superconductivity on surfaces of $\text{LiTi}_2\text{O}_4(111)$ thin films. *Nat. Commun.* **8**, 15975 doi: 10.1038/ncomms15975 (2017).

Publisher's note: Springer Nature remains neutral with regard to jurisdictional claims in published maps and institutional affiliations.



Open Access This article is licensed under a Creative Commons Attribution 4.0 International License, which permits use, sharing, adaptation, distribution and reproduction in any medium or format, as long as you give appropriate credit to the original author(s) and the source, provide a link to the Creative Commons license, and indicate if changes were made. The images or other third party material in this article are included in the article's Creative Commons license, unless indicated otherwise in a credit line to the material. If material is not included in the article's Creative Commons license and your intended use is not permitted by statutory regulation or exceeds the permitted use, you will need to obtain permission directly from the copyright holder. To view a copy of this license, visit <http://creativecommons.org/licenses/by/4.0/>

© The Author(s) 2017